CASL-U-2014-0061-000

Power uprates
and plant life extension

Consortium for Advanced Simulation of LWRs

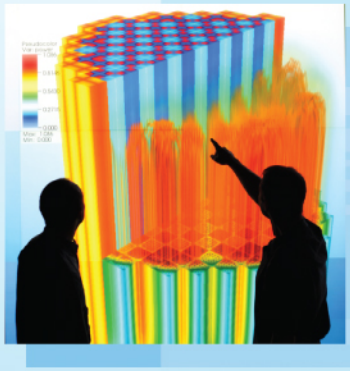

Engineering design
and analysis

Milestone L3:MPO.GTRF.P7.04

Assessment of modeling GTRF gap development

Hai Wang, Zupan Hu, Wei Lu and Michael Thouless
University of Michigan

Science-enabling
high performance
computing

March 20, 2014

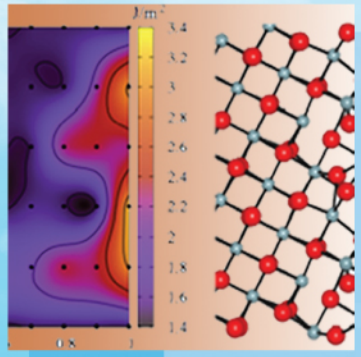

Fundamental science

Plant operational data

CASL-U-2014-0061-000

U.S. DEPARTMENT OF ENERGY | Nuclear Energy

Assessment of modeling GTRF gap development

Report to CASL / MPO - September 2013

Hai Wang, Zupan Hu, Wei Lu and Michael Thouless

University of Michigan

Ann Arbor, MI

Summary

In a previous report, we documented the development of a model to calculate the contact stress and gap evolution between the pin and the cladding. This model was incorporated into the finite-element code ABAQUS. This framework included the effects of creep, irradiation growth and thermal expansion in zircaloy, and creep, swelling, densification, and thermal expansion in the fuel. However, with the exception of the creep model, for which we had previously developed a mechanistic-based framework (although it was noted that data for diffusional creep, which are important for the evolution of contact stresses are not well documented), the models for the other phenomena were empirical equations taken from those provided by Matpro. In the past year, we have attempted to use the literature to develop a suitable equation for irradiation growth of polycrystalline zircaloy. The data and models in the literature appear to be insufficient to develop a mechanism-based model, especially as single crystal models don't seem to be appropriate for polycrystalline materials. We did develop a revised equation for steady-state irradiation growth; but a missing component is an understanding of how the dislocation density evolves during service conditions.

One phenomenon missing in the previous analysis of gap formation was hydride formation. Since another group at the University of Michigan is working on phase-field models of hydride formation, we decided to explore what would be needed to link these lower-length scale models with continuum-level models of gap evolution. Such a framework has been developed that links hydrogen diffusion and concentration, stress, temperatures, and local hydride concentration to further hydride growth. The framework further links this hydride growth and local texture to the development of local stresses, the relaxation of these stresses by creep mechanisms, and the eventual link back to how these relaxed stresses affect hydride growth. We report how the linking of length scales might be done with the interaction of all these effects at a continuum level of analysis of a grid/rod structure, and we present with some preliminary results. However, the major obstacle to implementation appears to be the lack of a correct energy potential for the Zr-H; the lower-level results currently do not seem to yet yield correct equilibrium values that would correlate with a known phase diagram. An additional missing input from the lower level is information on the dissolution of hydrides.

CASL-U-2014-0061-000

1. Introduction

There are two approaches to multi-scale modeling of the gap formation in the GTRF problem: bottom-up or top-down. The bottom-up approach starts the modeling at the atomistic scale moving up through the grain to the structural level. The top-down approach starts off with a continuum model of the structural level and reaches down in a phenomenological fashion to pull needed information up from lower-level scales on an as-needed basis.

One inherent problem with bottom-up models is that one does not necessarily know *a priori* what phenomena and modeling details at the lower-length scales need to be captured to describe the behavior at much larger engineering scales. Conversely, an approach in which one starts off at the engineering scale of interest allows one to identify the lower-length scale phenomena that need to be included much more readily. Furthermore, there are scales below which the details of the geometry and microstructure can only be described in average terms of the ensemble; considerations of efficiency for design and analysis would seem to argue for effects controlled by features at this scale to be described by averaging techniques up at the macroscopic scales. For these, and other reasons, we are focusing on developing a continuum-level framework for GTRF, and trying to understand how to reach down to models developed at the lower-length scales on an as-needed basis.

This general approach was presented in a previous report by the group [Wang *et al.*, 2012]. This report presented a model implemented in ABAQUS analyzing the evolution of the grid-to-cladding gap and the contact pressure during service as a pin is moved from the inner to the outer regions in the core of a pressurized-water reactor

(PWR), in three fuel cycles. The starting point of this model was a multi-mechanism creep model for zircaloy [Wang, *et al.*, 2013], that had been developed by analyzing the creep literature for zircaloy over the past four decades and interpreting it in terms of established mechanism-based models for creep. Incorporation of this model into a finite-element code allowed the appropriate stress-relaxation mechanisms to evolve naturally as temperatures and stresses evolved. One important message that came from the analysis of the experimental data in the literature was that the role of texture is not important for creep driven only by stress. In the previous report, we also demonstrated the addition of modules to inlcude irradiation swelling of the fuel, irradiation growth of the zircaloy (which did include the effects of texture), and densification of the fuel under pressure. The report presented the results of the gap evolution calculated using a 2-D ABAQUS model of a typical pin / grid assembly, in which the phenomena of creep-down of the clad onto the fuel, fuel swelling, thermal expansion and contraction, irradiation growth and creep of the grid and clad, mechanical interaction between fuel and clad, along with creep of the fuel and creep-relaxation at the clad/grid contact were all allowed to interact. It was observed that the two phenomena that dominated the evolution of the contact stresses at the pin-clad interface were the swelling of the fuel, and the creep mechanisms of the zircaloy.

Other than the creep model that we had developed, useful mechanism-based models for use at the continuum scale were not available to us. Therefore, we simply implemented the phenomenological equations from Matpro [Allison *et al.,* 1993]. However, it should be recognized that these equations appear to be severely lacking in their ability to capture the general physics of the behavior, making them of limited use for analysis. A

comparison with the published literature suggested this was especially true for irradiation growth in polycrystalline materials. Furthermore, it appeared that single-crystal models are of limited use in predicting the behavior of polycrystalline zircaloy.

Since the submission of the last report, four issues were identified that needed to be addressed further. (i) Whether the Sierra package can be used / modified to allow the approaches we developed for ABAQUS to be implemented in Sierra. (ii) Whether there are sufficient data that are described sufficiently in the literature to develop mechanism based models for radiation effects on creep that are of the same caliber as the stress-based creep models. (iii) Whether one could incorporate a mechanism-based model of hydride growth into the GTRF analysis. Each of these three issues have been addressed to various levels during the past year. However, as will be described in more detail later in the report, it is the final issue that we have decided to focus our attention on, as it meshes with lower length-scale models being developed at the University of Michigan (UM). By focusing on this problem, and collaborating with the Thornton group at UM, we hope eventually to provide an example of multi-scale analysis in which a continuum-level analysis uses and interacts with calculations provided at lower length scales. At this time, this is on-going work, but we think we have set the framework in place for this to be refined over the coming year.

After comparing the experimental data and the results calculated from the equation of irradiation growth from Matpro, we find the equation fail to describe the long-term behavior of zircaloy in radiation. Therefore, we search the literature for data and try to give a better expression for irradiation growth, which is discussed in this report.

2. Interaction with Sierra

Subroutines used in ABAQUS to implement the effects of creep, thermal expansion, irradiation growth in Zircaloy and creep, swelling, sintering, and thermal expansion were sent to Nathan Crane at Sandia for implementation in Sierra in the spring. We have had no further requests for input.

3. Irradiation growth

Irradiation growth is the shape change that occurs at constant volume during irradiation of an unstressed material. This is an anisotropic dimensional change that occurs during neutron irradiation. The results of the model for gap formation indicate that the effect of irradiation growth is negligible so, at some level, one could argue that development of a high-fidelity model is not a high-priority concern for this problem. Despite this consideration, we did spend time exploring the literature to evaluate the level of understanding of this phenomenon as appropriate for a continuum-level approach to GTRF. This study had three parts: (i) a comparison between single crystal data and polycrystalline data to see if single crystal models could be used; (ii) a comparison between the empirical equation used by Matpro and experimental data on the literature to see the extent to which the Matpro equation captured the behavior; (iii) the development of a preliminary and approximate phenomenological equation that described the data. A major conclusion of this work is that the Matpro equation does not seem to be a good description of steady-state irradiation growth. Based on the data in the literature we have developed an alternative expression for steady-state growth - but, the effects of grain size and the relationship between the extent of cold work and dislocation density is missing.

3.1 Irradiation growth of single crystal zircaloy

Growth of an annealed single crystal has an expansion parallel to the *a*-axis and a contraction along the *c*-axis [Carpenter *et al.*, 1981; Carpenter *et al.*, 1988]. To relate anisotropic strains in a single crystal to strains in a polycrystalline material, one has to relate them to the average texture of the material. The texture, f_i, is defined as the fraction of basal poles in the *i*-direction:

$$f_i = \left\{ \int_V \cos^2 \theta_i dV \right\} / V, \tag{1}$$

where θ_i is the angle between the c-axis of an individual grains and the reference direction, *i*, and *V* is the volume. The strain in the *i*-direction is then given by

$$\varepsilon_i = (1 - f_i)\varepsilon_a + f_i \varepsilon_c, \tag{2a}$$

where ε_a and ε_c are the strains in the basal and axial directions. For irradiation growth, which occurs at constant volume, $2\varepsilon_a + \varepsilon_c = 0$, so that the irradiation strain is given by [Harbottle and Cornell, 1977; Allison *et al.*, 1993]

$$\varepsilon_i = (1 - 3f_i)\varepsilon_a, \tag{2b}$$

where ε_a is the expansion in the basal direction. In principle, it should be possible to use this expression to predict irradiation growth in polycrystals from single-crystal data or models. Unfortunately, a comparison between single-crystal data and polycrystalline data shows that the actual growth strains of polycrystalline zircaloy are much bigger than those that would be expected from single crystal data. It would appear that grain boundaries provide an important component to irradiation growth in polycrystalline zircaloy [Carpenter *et al.*, 1988], and single crystal models may be of limited utility for incorporation in continuum models of gap formation.

3.2 Irradiation growth of the polycrystalline zircaloy

The irradiation growths of annealed and cold-worked-and-stress-relieved (CWSR) polycrystalline zircaloy show different behavior. Annealed zircaloy generally exhibits three stages of irradiation growth: transient, steady state, and "breakaway" growth [Holt and Gilbert, 1986]. The strain rate remains constant in the steady-state regime, and rapidly increases in the "breakaway" regime. In contrast, CWSR zircaloy material generally exhibits only two stages: transient and steady state. For example, some experimental data for irradiation growth of CWSR zircaloy is shown in Fig. 1.

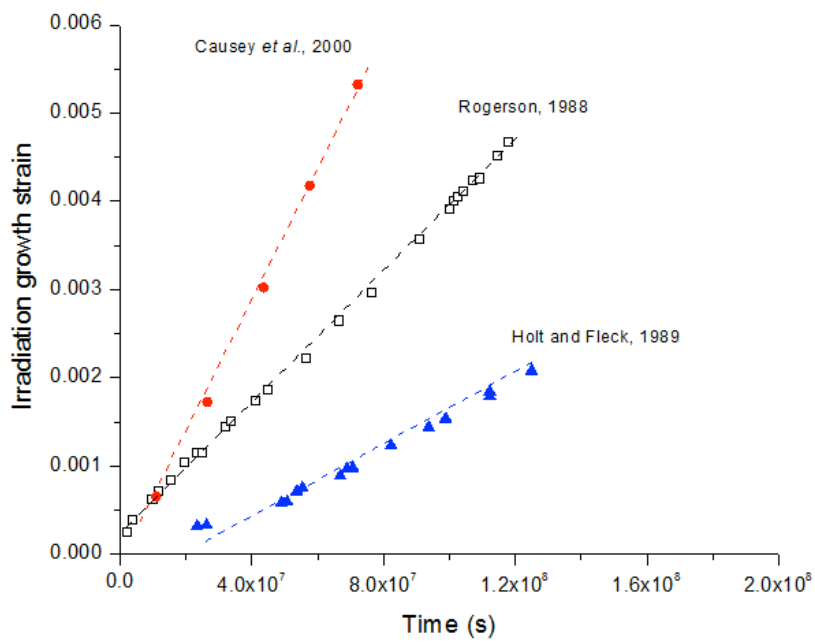

Figure 1 Irradiation growth strain increases linearly with time at steady state for the cold-worked-and-stress-relieved Zircaloy at constant levels of neutron flux.

3.3 Comparison between experimental data and the equation from Matpro

MATPRO gives an equation for the irradiation growth in an arbitrary direction i, in terms of the texture in that direction, f_i, the amount of cold-work, CW (in %), the temperature, T

(in K), and the total fast neutron fluence, ψ (in neutrons / m^2). Implementation into a finite-element framework requires an expression for the strain *rate* in terms of instantaneous flux and the total fluence experienced by an element of the material. The equation from MATPRO [Allison *et al.*, 1993] can be differentiated to give such an expression:

$$\dot{\varepsilon}_i = 7.0 \times 10^{-17}\left[\exp(240.8/T)\right]\dot{\psi}\psi^{-1/2}(1-3f_i)(1+2CW) \qquad (3)$$

The predictions of this equation were compared to results in the literature for irradiation growth of polycrystalline zircaloy for different temperatures and cold work (Fig. 2). These comparisons indicate that this empirical expression does not describe the long-term behavior of zircaloy during radiation. It may be a better description of the initial transient effects.

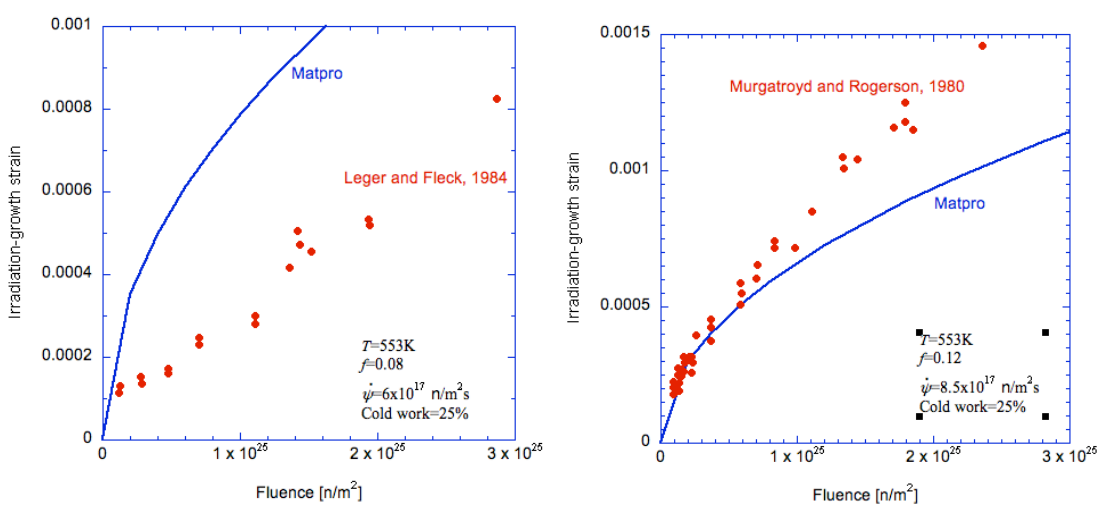

(a) Data from Leger and Fleck [1984]. **(b)** Data from Murgatroyd and Rogerson [1980].

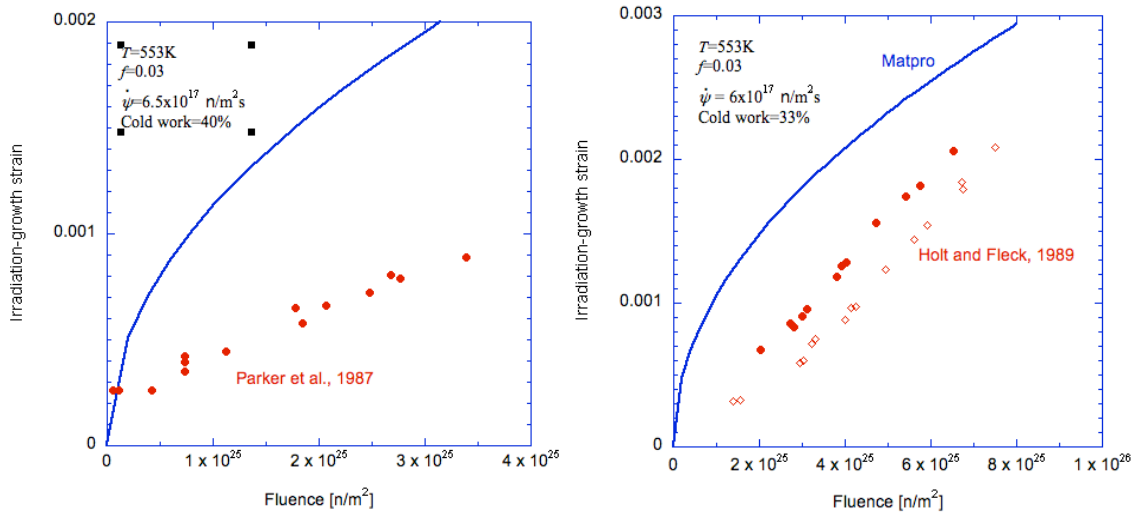

(c) Data from Parker *et al.* [1987] **(d)** Data from Holt and Fleck, 1989

Figure 2 Comparison between experimental data and the equation from Matpro [Allison *et al.,* 1993].

3.4 Development of a new phenomenological equation for irradiation growth

Unfortunately, there appear to be no mechanistic models of irradiation growth for *polycrystalline* zircaloy, and the single-crystal models do not seem to provide a good description of the polycrystalline behavior. Furthermore, the empirical expression given by Matpro seems to be of limited utility in its ability to describe experimental data given in the literature. What is given below is the development of a phenomenological equation for irradiation growth based on available experimental data. In this context it should be noted that the useful data for developing irradiation growth data (independent of creep-radiation interactions) is somewhat limited.

3.4.1 Texture

As discussed above, irradiation growth strain along a specific direction, i, follows the $(1-3f_i)$ rule, where f_i is the texture [Harbottle and Cornell, 1977; Allison *et al.*, 1993]. Although others propose different dependence of irradiation growth on texture [Causey *et*

al., 1988; Holt, 1979], here the expression involving (1-3f_i) is used, because of its sound basis in anisotropic analyses and its simplicity.

3.4.2 Dislocation density

The "breakaway" phenomenon observed in annealed zircaloy is caused by the nucleation and growth of <*c*>-component dislocation loops on the basal plane [Holt and Gilbert, 1986]; this demonstrates the importance of dislocation density, ρ, on irradiation growth. Data measured at the same temperature and flux are plotted together, and the effect of texture is eliminated by plotting $\dot{\varepsilon}/(1-3f)$ against the dislocation density in Fig. 3. This shows the approximately linear relationship, $\dot{\varepsilon} \propto \rho^{1.1\pm0.3}$, between dislocation density and growth rate that has been previously reported [Holt, 1979; Holt, 1980].

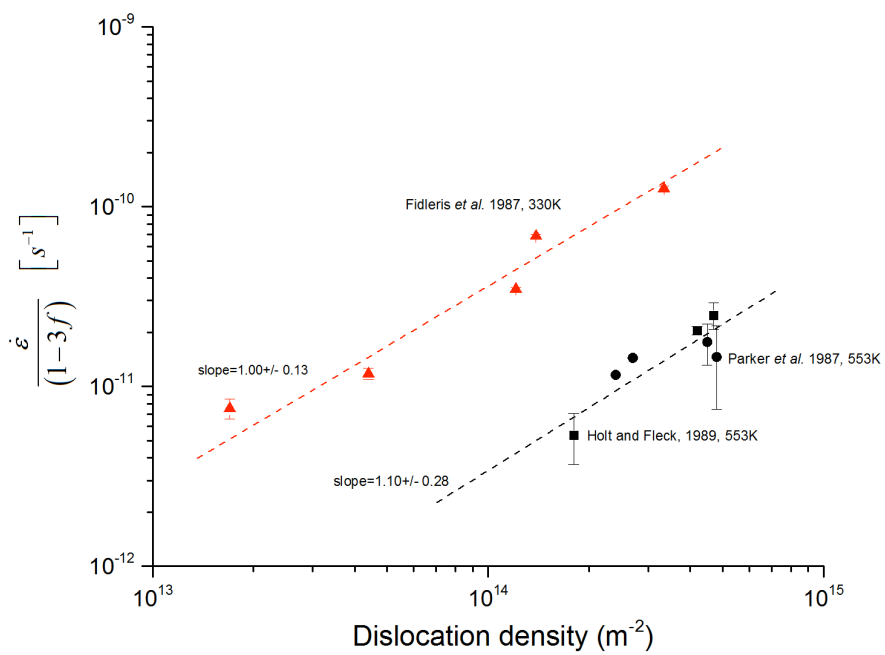

Figure 3 $\dot{\varepsilon}/(1-3f)$ plotted against the dislocation density showing an approximately linear relationship between growth rate and dislocation density.

3.4.3 Fluence

The dependence of irradiation growth strain on neutron fluence, ψ, from different sources is shown in Fig. 4. This shows a similar result to the data of Fig. 1 and 2, in that the growth strain in steady state is linearly dependent on the fluence, or the strain rate is proportional to the flux. The results for the effect of fluence, texture and dislocation density on irradiation growth indicates a general expression of

$$\dot{\varepsilon} = A\dot{\psi}(1-3f)\rho^{1.1} \quad , \tag{4}$$

where A is an empirical constant. This expression can be used to explore the effects of temperature. By plotting $\dot{\varepsilon}/\dot{\psi}(1-3f)\rho^{1.1}$ for sets of data taken from the literature at different temperatures, one can explore if there is a systematic effect of temperature. This is done in Fig. 5.

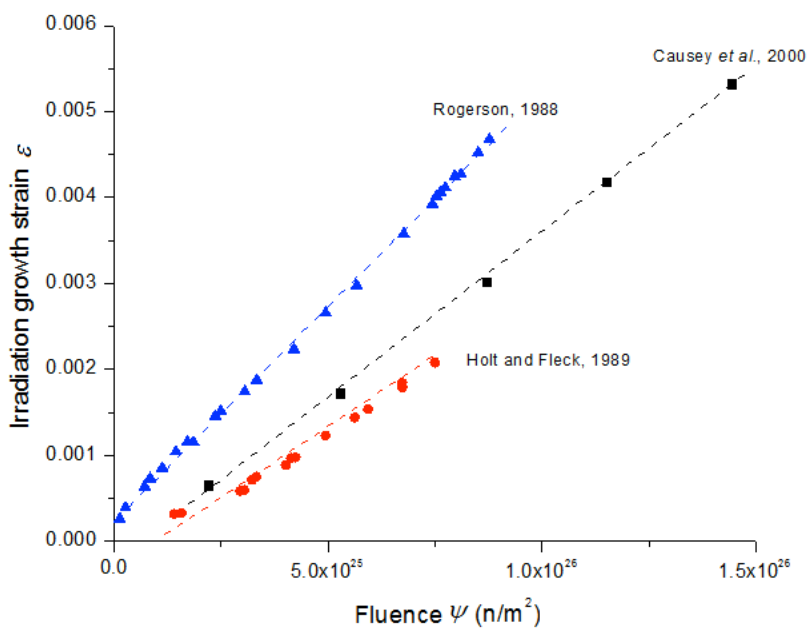

Figure 4 Irradiation growth strain is plotted against fluence. The irradiation growth strain depends linearly on the fluence.

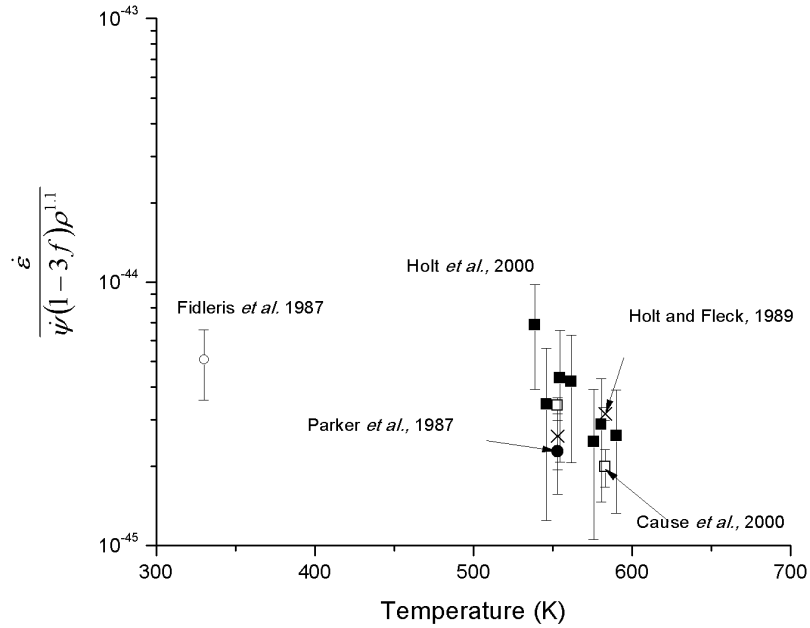

Figure 7 $\dot{\varepsilon}/\dot{\psi}(1-3f)\rho^{1.1}$ is plotted against temperatures. No obvious trend is observed, which suggests the dependence on temperature is weak.

Similar conclusions on the relative independence of temperature were also obtained by other researchers [Ibrahim and Winegar, 1972/73; Holt, 1979]. The effect of temperature is, therefore, not included in the proposed in phenomenological equation for irradiation growth

3.4.4 Phenomenological equation for steady-state irradiation growth

Using the experimental data plotted in Fig. 5 to deduce the empirical parameter A of Eqn. 4, leads to the following expression for the steady-state irradiation-growth strain rate in any arbitrary direction:

$$\dot{\varepsilon}_i = (3.5 \pm 2.4) \times 10^{-45} (1 - 3f_i) \rho^{1.1 \pm 0.3} \dot{\psi} \qquad (5)$$

The data does not appear to exist that would allow one to include the effects of grain size (or grain boundary area per unit volume) into the expression. Furthermore, models that allow dislocation density to be identified with macroscopic parameters such as the degree

of cold work, annealing before service, and how the dislocation density changes during service have not been identified. These are remaining challenges that need to be addressed before being added to deformation models of zircaloy. However, as discussed earlier, the gap formation does not appear to be sensitive to this phenomenon, so this may not be a high priority to address for this problem.

Note that since attempting this semi-empirical approach for irradiation growth, we have developed the framework described below for hydride growth which uses the results from a model based at a single crystal level directly at a continuum-level analysis, including the effects of anisotropy and texture. The framework would be equally useful for a single-crystal model of irradiation growth, provided that the dislocation density and neutron flux at every element could be described at the continuum level.

4. Hydride Growth

One important module missing from the framework presented in the previous report [Wang *et al.*, 2012] was the effect of hydride formation on the evolution of the gap. Hydrogen, which is the product of water-zirconium reaction on the cladding surface, diffuses into the cladding and forms a hydride ($ZrH_{1.66}$). The hydride usually forms in the basal plane of the crystal, and is associated with a volume expansion of about 17%. It is expected that at high hydride concentrations this volume expansion may significantly affect the dimensions of the cladding and the gap between the pin and cladding. Furthermore, internal stresses set up by the volume changes may also affect the deformation, and lead to failure. Conversely, these internal stress are also expected to interact with the hydride growth mechanisms, but the will also relax as a result of the creep mechanisms that occur. The goal of this project was to incorporate hydride growth into the gap-formation model and couple the interactions between hydrogen diffusion, hydride nucleation and growth, stress evolution, and stress relaxation using the creep mechanisms previously incorporated into the model. A second goal of this project was to use this study as a vehicle to demonstrate an interaction between models of phenomena at different time and length scales, which forms an inherent part of the general goal of CASL. To this end, a collaboration has been established between the Thouless/Lu and Thornton groups at the University of Michigan, to establish a framework by which low-length scale models for hydride growth/nucleation can interact with a continuum-level model of the pin-clad assembly which incorporates the effects of creep and long length and time scales. At this stage (September 2013), a framework has been established for the interaction between HYRAX and ABAQUS. This has been demonstrated for a very

small subset of results from HYRAX. The current lack of a suitable set of results from the lower-length scale has limited our ability to demonstrate how the model will accommodate stress and temperature, but these are expected shortly. Of more significance seems to be the input, in the form of the H-Zr interaction energies, into the phase-field models that seem to be limiting the accuracy of the output being used by the continuum model. Currently these are taken from the literature [Guo *et al.*, 2008] - but, as will be clear in the discussion below, these energies don't give the correct equilibrium phase diagram for Zr-H. However, we use these results, since we want to focus on how to make a connection between different levels, and to get experience with the type of output that HYRAX can produce.

Since local stresses, hydrogen concentration, temperature and volume fraction of hydride all have an effect on the evolution of hydrides, values of these parameters are stored for every element in the simulation. In each time step, the stresses are updated using the creep model presented earlier. The temperature is updated according to thermal conductivity and boundary conditions. The hydrogen concentration is updated using a diffusion model based on the concentration gradient between neighboring elements. The hydride volume fraction is updated following using input from HYRAX. Details of this framework are elaborated below, with some examples of results from initial calculations.

4.1 Hydrogen diffusion

Water reacts with zirconium on the surface of the cladding to produce oxide and hydrogen. Hydrogen diffuses through the cladding from the surface, and reacts with zirconium to form hydride. Therefore, to calculate how much hydride forms, it is necessary to simulate hydrogen diffusion and to compute the hydrogen concentration at

different locations based on given boundary conditions (which is beyond the scope of this present framework, but will be required as input from another level of calculation). The governing equation for hydrogen diffusion is

$$\frac{\partial c_H}{\partial t} = D_x \frac{\partial^2 c_H}{\partial x^2} + D_y \frac{\partial^2 c_H}{\partial y^2} + D_z \frac{\partial^2 c_H}{\partial z^2} \tag{6}$$

where c_H is hydrogen concentration and D_x, D_y and D_z are the 3-D components of the diffusion coefficient. Here it is assumed that the hydrogen diffusion is isotropic, so the components are identical. The hydrogen concentration gradient is considered to be the only cause for diffusion. The effects of temperature gradients and stress gradients on the hydrogen diffusion are ignored, but can be added if required.

Equation 6, a partial differential equation, is the strong form of hydrogen diffusion. The strong form is transformed into the weak form, which is the integration over the elements. The strong and weak forms are equivalent, and the finite-element analysis is based on the weak form of the diffusion equation. The cladding is discretized over space to generate a mesh (which is also used for the other calculations). The information of the mesh, such as the coordinates of the nodes and element connectors, are acquired from URDFIL, an ABAQUS subroutine used to read the result file of a simulation. The element connector provides the information about which nodes are in a specific element. By using the proper linear basis functions, integration points, weight functions and isoparametric mapping, element integration is computed, and the corresponding element-stiffness matrix is constructed. Finally, all the element-stiffness matrices are assembled into a global system-stiffness matrix, which is generally known as [K].

The boundary conditions are expressed in terms of an assumed hydrogen flux at the surfaces. (For example, this might be a constant flux at the surface of the cladding that is in contact with water, and no flux at the surface contacting the fuel. Or, one could incorporate a diffusivity of the fuel.) The boundary-condition vector, **F**, is computed for each element that lies on the boundary.

Hydrogen diffusion is a transient problem, so there is another global matrix which counts for the change of hydrogen concentration. This matrix is denoted by [*M*]. The procedure for computing this matrix is similar to that for computing [*K*]. The element matrix is constructed with proper linear basis functions, integration points, weight functions and isoparametric mapping first and then they are assembled to get the global matrix, [*M*]. Lastly, the weak form is transformed into the time-dependent hydrogen diffusion equation.

$$[M]\frac{\partial \mathbf{c}_H}{\partial t} + [K]\mathbf{c}_H = \mathbf{F} \tag{7}$$

The dimension of [*K*] and [*M*] is $N \times N$, where N is the number of nodes, and the dimension of $\mathbf{c}_H$, the vector of the hydrogen concentrations at each node, and of **F** is $N \times 1$. To solve this time-dependent equation, the explicit method and the mid-point rule of Euler method are adopted to guarantee accuracy and unconditional stability. Finally, this equation is solved to obtain the hydrogen concentration for each node at each time increment.

Additionally, the hydrogen concentration for each element in the mesh is be calculated by averaging the hydrogen concentrations at the nodes that are in this element. For the 3-D model, there are 8 nodes in an element, while there are 4 nodes in an element of a 2-D

model. The hydride volume fractions at different locations are then calculated based on this hydrogen concentration, as discussed below.

4.2 Hydride volume fraction calculation

The hydride will begin to form in the cladding after the hydrogen concentration reaches the saturated value. The hydrostatic stress, temperature, time, hydrogen concentration and volume fraction of hydride, all affect the nucleation and growth of the hydride. Prof. Thornton's group conducts a phase-field simulation of the process. Only δ-hydride forming in the basal plane is considered, and it is assumed that the stress state does not change its habit plane. The form of the data that Prof. Thornton's group can provide us with is plots of hydride evolution in a single crystal as a function of time at fixed total hydrogen concentration, temperature and the biaxial stress state in the basal plane (assuming zero stress in the axial direction). We have developed a continuum-level approach to take out-put from the phase-field models of this form, and incorporate it into a larger scale finite-element calculation in the hydrogen concentration, stresses, and temperatures can vary continuously in region of polycrystalline zircaloy with a given texture.

The basic framework of this approach is that the relevant parameters (total hydrogen concentration, temperature, stress, and current volume fraction of hydride) for an element are calculated at the beginning of a time increment. These parameters are matched to the appropriate set of phase field results showing how the hydride evolves with time at a fixed stress, temperature and hydrogen concentration, to find the growth rate. The appropriate curve is used to update the volume fraction of hydride at the end of the time increment (with the free hydrogen in the element reduced accordingly). Changes in the

free hydrogen concentration during the time increment are also calculated by applying the diffusion equation to any hydrogen that is not associated with the hydride. Any change in stress owing to the additional hydride formation is calculated, and creep relaxation is allowed to occur during the time increment according to the creep models. If there are any thermal gradients, the temperature of all the elements is also updated during the time increment. Once all the parameters have been updated, the calculation moves on to the next time increment. Further details are given below, along with an example of some preliminary results.

4.3 Strain associated with hydride formation

The strain tensor associated with the hydride formation depends on the volume fraction of the hydrides, F_{ZrH}, and the local texture of the cladding. The texture of the cladding is referenced to three local orthogonal axes, i, j and k. (In the axisymmetric geometry of cladding, these local axes are conveniently equated to the appropriate cylindrical co-ordinate system.) The texture is specified by three values, f_i, f_j and f_k, where f_i is the effective volume fraction of grains whose <*c*>-axis is parallel to the *i*-direction, f_j is the effective volume fraction of grains whose <*c*>-axis is parallel to the *k*-direction, and f_k is the effective volume fraction of grains whose <*c*>-axis is parallel to the *k*-direction. For simplicity, it is assumed that the grains are oriented in one of only three ways, with the <c>-axes being parallel to one of the three local directions. Consequently, the volume fractions of grains oriented in these three directions are f_i, f_j and f_k, respectively.

The last input required to calculate the strain tensor of each node is the misfit strains of δ-hydride ($ZrH_{1.66}$) forming in the basal plane. The temperature-dependent misfit strains are reported as [R. N. Singh, et al., 2007]:

$$m_{aa} = 0.03888 + 2.315 \times 10^{-5} T \tag{8a}$$

$$m_{cc} = 0.06646 + 1.9348 \times 10^{-5} T \tag{8b}$$

where, m_{aa} is the misfit strain in the basal plane, m_{cc} is the misfit strain normal to the basal plane, and T is the temperature in K.

The local strain at each node is calculated first. The volume fraction of hydride forming in each grain is a function of the hydrostatic stress in the basal plane, temperature, and hydrogen concentration. The temperatures and the hydrogen concentration are the same for grains in any orientation, but the hydrostatic stresses in the basal planes are different. The result file of ABAQUS gives the three normal stresses in Cartesian co-ordinates (*x, y, z*) for each node. These can be transformed using standard equations for the transformation of stresses to the appropriate local co-ordinate system (*i, j, k*) with which the texture is referenced through Eqn 1.

The volume fraction of grains aligned with the basal plane normal to the *i*-direction is f_i (Eqn. 1), and the hydrostatic stress in the basal plane of these grains is $(\sigma_{jj} + \sigma_{kk})/2$; the volume fraction of grains aligned with the basal plane normal to the *j*-direction is f_j, and the hydrostatic stress in the basal plane of these grains is $(\sigma_{ii} + \sigma_{kk})/2$; the volume fraction of grains aligned with the basal plane normal to the *k*-direction is f_k, and the hydrostatic stress in the basal plane of these grains is $(\sigma_{ii} + \sigma_{jj})/2$. In general, these different stresses will result in different rates (and equilibrium values) of hydride formation in each orientation (as given by the appropriate calculations for single grains in the phase-field analyses). Therefore, at any instant in time, there will be different volume fractions of

hydrides, F_i, F_j, and F_k, in each of these grain orientations. The total volume fraction of hydride in any element is given by

$$F_{ZrH} = f_i F_i + f_j F_j + f_k F_k \tag{9}$$

The crystallographic strains associated with the formation of the hydride in the three different orientations of grains are

$$\begin{aligned} \varepsilon_{aa}^{i} &= F_i \times m_{aa}; \quad \varepsilon_{cc}^{i} = F_i \times m_{cc} \\ \varepsilon_{aa}^{j} &= F_j \times m_{aa}; \quad \varepsilon_{cc}^{j} = F_j \times m_{cc} \\ \varepsilon_{aa}^{k} &= F_k \times m_{aa}; \quad \varepsilon_{cc}^{k} = F_k \times m_{cc} \end{aligned} \tag{10}$$

The macroscopic strains can then be determined from the textures in the three different directions:

$$\varepsilon_i = \varepsilon_{cc}^{i} f_i + \varepsilon_{aa}^{j} f_j + \varepsilon_{aa}^{k} f_k \tag{11a}$$

$$\varepsilon_j = \varepsilon_{aa}^{i} f_i + \varepsilon_{cc}^{j} f_j + \varepsilon_{aa}^{k} f_k \tag{11b}$$

$$\varepsilon_k = \varepsilon_{aa}^{i} f_i + \varepsilon_{aa}^{j} f_j + \varepsilon_{cc}^{k} f_k \tag{11c}$$

where ε_i, ε_j and ε_k are the strains in the i, j, and k directions. These strains are then transformed back to the Cartesian co-ordinates by the usual transformation equation for use in the ABAQUS subroutine. These strains are the strains at a particular node, so the strain of an element is calculated by averaging the nodal strains for each element. These averaged strains are input into ABAQUS subroutine UEXPAN to compute the deformation of the cladding and, hence, the stress distribution associated with hydride formation.

5. Results

5.1 Data from lower-length scale simulation

As an initial example, we were provided by three simulations were conducted by A. Jokisaari at the University of Michigan, to illustrate the format in which the data from the

phase-field calculations could be obtained for the finite-element calculations. The results are shown in Fig. 8.

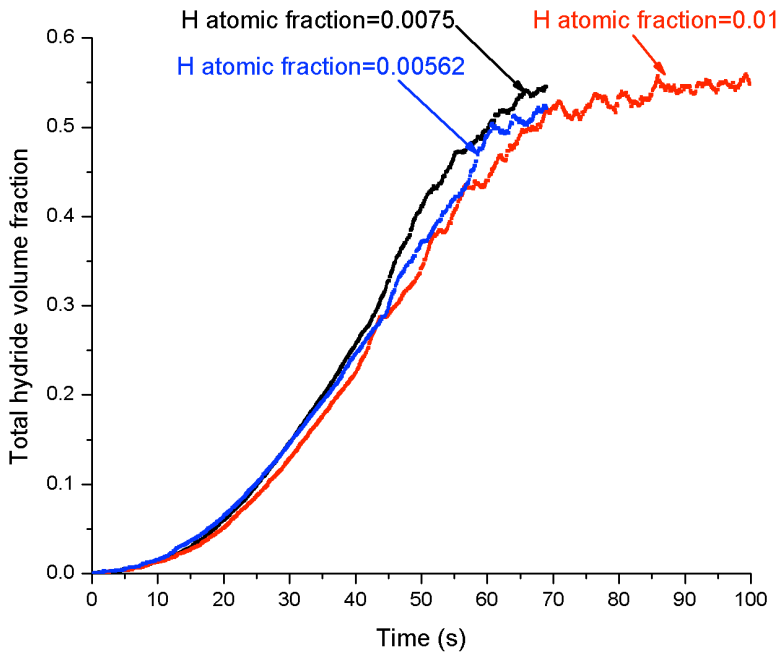

Figure 8 Total hydride volume fraction is plotted against time at three different H atomic fractions. (Data provided by A. Jokisaari from phase-field calculations.)

It should be noted that the correct free-energy function does not seem to be yet available as an input to these phase-field calculations. Therefore, the results shown in Fig. 8 are not parameterized to realistic hydride data. However, we still decide to analyze the data, and run the simulations at continuum level to show what would be possible if accurate data were available. The range of hydrogen concentrations were limited in the results of Fig. 8, so we extrapolated the data that was provided to provide the full range required. The extrapolated hydride growth data that was used as the basis for the finite-element calculations is shown in Fig. 9. We did not attempt to estimate what the effects of

temperature and stress would be. We therefore assumed that the curves of Fig. 9 are valid for all stress states and temperatures.

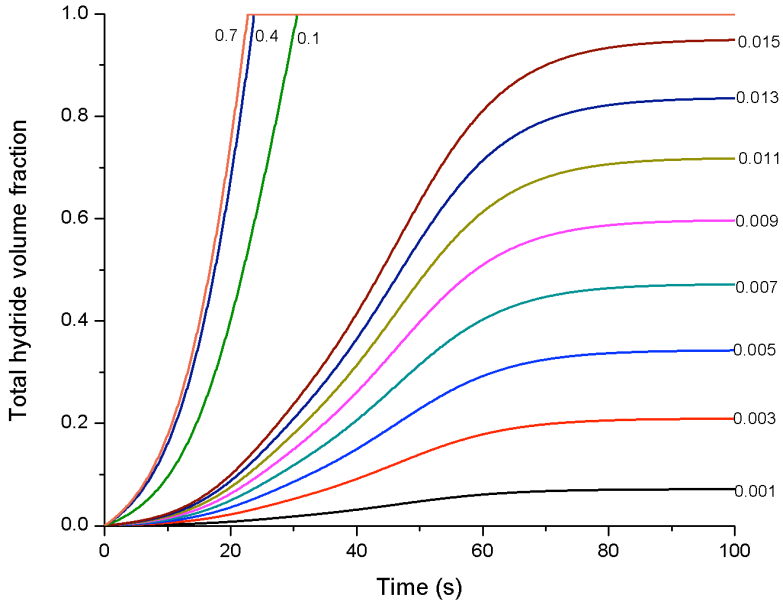

Figure 9 Hydride formation at different H atomic fractions, as used in the finite-element calculations.

5.2 Results of the continuum-level simulation

A three-dimensional model is constructed in ABAQUS in which only one quarter of the cladding was considered. Using cylindrical co-ordinates (r, h and z) for the cladding, the texture was assumed to be f_r=0.66, f_h=0.28, and f_z=0.06. The total time for the simulation was 1×10^5 s. The initial time step is 3s, and the maximum time step is 500s. A hydrogen influx of 1×10^{-6} [ppm·m/s] was assumed on the outer surface of the cladding.

The mechanical and thermal boundary conditions are given in Fig. 10.

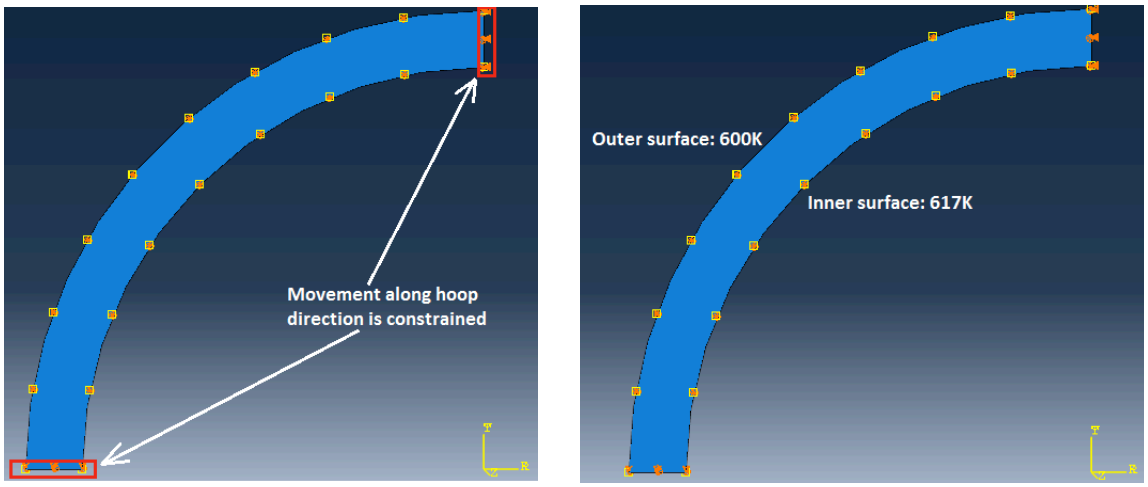

(a) (b)

Figure 10 (**a**) Mechanical boundary conditions: quarter-plane symmetry was assumed, with movement along the hoop direction of the two edges is constrained. **(b)** Thermal boundary conditions. The temperature of the outer surface is 600K and the temperature of the inner surface is 617K [Wang *et al.*, 2012] Thermal expansion is not considered in this model.

5.2.1 Results

The calculations were first performed without considering the effects of creep. These results are shown in Figs. 11 and 12 for the volume fraction distribution and elastic stress distribution, respectively. Then, the calculations were repeated with the creep mechanisms switched on. Since no effect of stress on hydride formation was assumed, the hydride formation was unchanged. However, the effect of creep on the stress state induced by the non-uniform volume expansion of the hydride can be seen in Fig. 13. The last set of calculations done were with a new texture (f_r=0.34, f_h=0.33, and f_z=0.33), but no creep is switched off. The resultant von Mises stress is shown in Fig, 14.

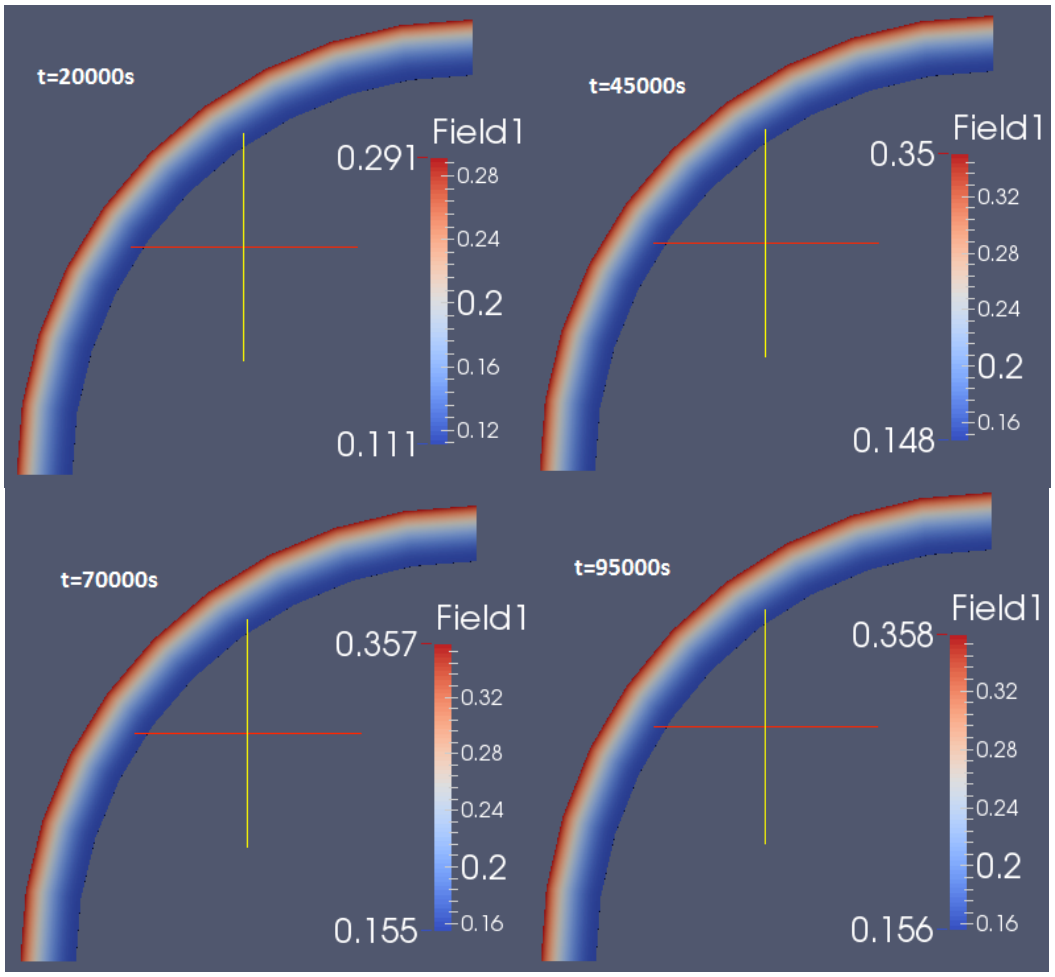

Figure 11 Hydride volume fraction distributions at different times. **(a)** *t*=20000s; **(b)** *t*=45000s; **(c)** *t*=70000s; **(d)** *t*=95000s; As time increases the hydride volume fraction increases. Since the hydrogen influx is on the outer surface of the cladding, the hydride volume fraction at the outer perimeter is larger than that inside.

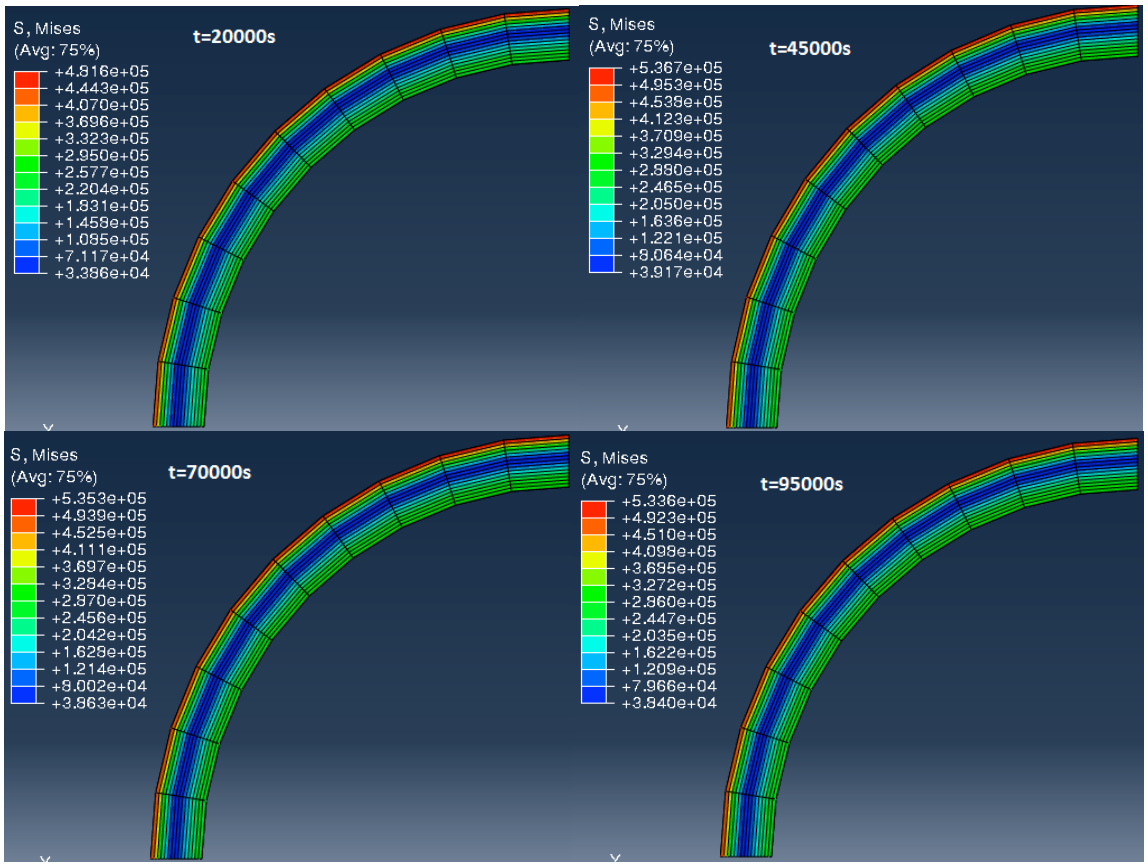

Figure 12 von Mises stress distributions at different times. **(a)** *t*=20000s; **(b)** *t*=45000s; **(c)** *t*=70000s; **(d)** *t*=95000s; With more hydride forming in the cladding, the stress increases.

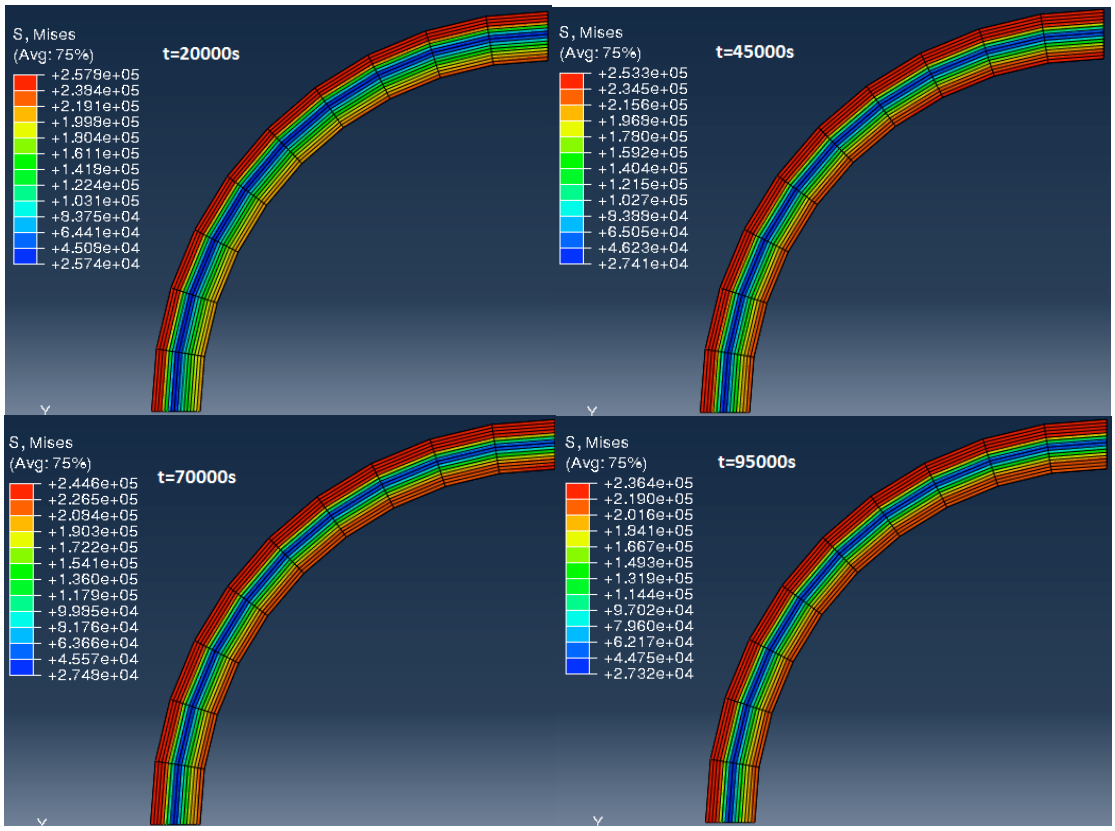

Figure 14 von Mises stress distributions at different times with creep switched on. **(a)** *t*=20000s; **(b)** t=45000s; **(c)** *t*=70000s; **(d)** *t*=95000s; In comparison with Fig. 13, stress relaxation is observed. The stress distribution evolves to a steady-state in which the rate of stress increase caused by hydride formation is the same as the rate of stress relaxation.

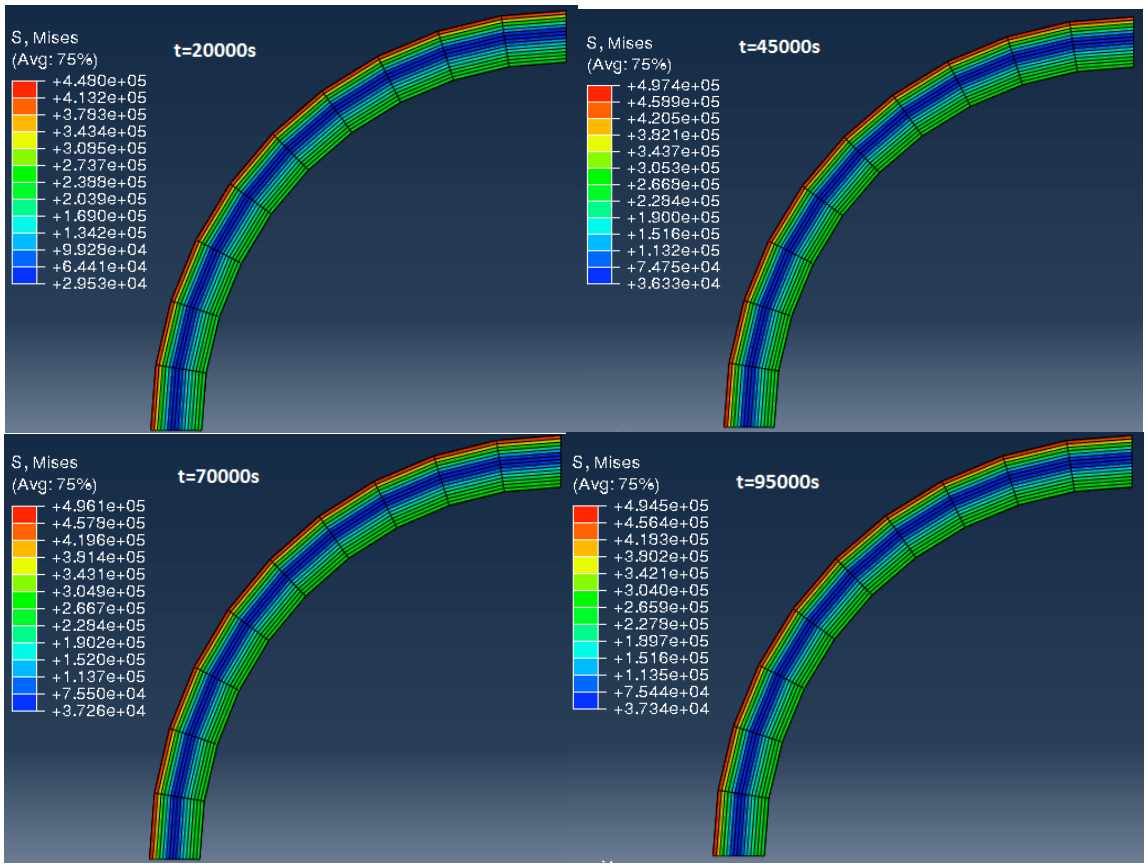

Figure 15 von Mises stress distributions at different times in the cladding that is isotropic. **(a)** *t*=20000s; **(b)** *t*=45000s; **(c)** *t*=70000s; **(d)** *t*=95000s; This set of figures should be compared with Fig. 13 to show the effect of texture on stress distribution. The comparison shows stress becomes smaller after changing the texture but the difference is not big. Therefore, if the effect of stress on hydride formation is considered later, the change of the texture will have an influence on the hydride formation.

6. Incorporation of hydride model into gap formation analysis

In this section we describe the incorporation of the hydride formation model into the original gap formation analysis of Wang *et al.* [2012]. Recognizing that we don't currently have useful lower-level data, we have had to develop an alternative formulation based on a published Zr-H phase diagram [Veshchunov and Berdyshev, 1998]. However, we assume that temperature and stress have no effect on the solubility of hydrogen in zirconium (although the framework would allow this information to be included). The

approximation to the phase diagram used is shown in Fig. 16, and the equilibrium hydride volume fraction is calculated based on this diagram.

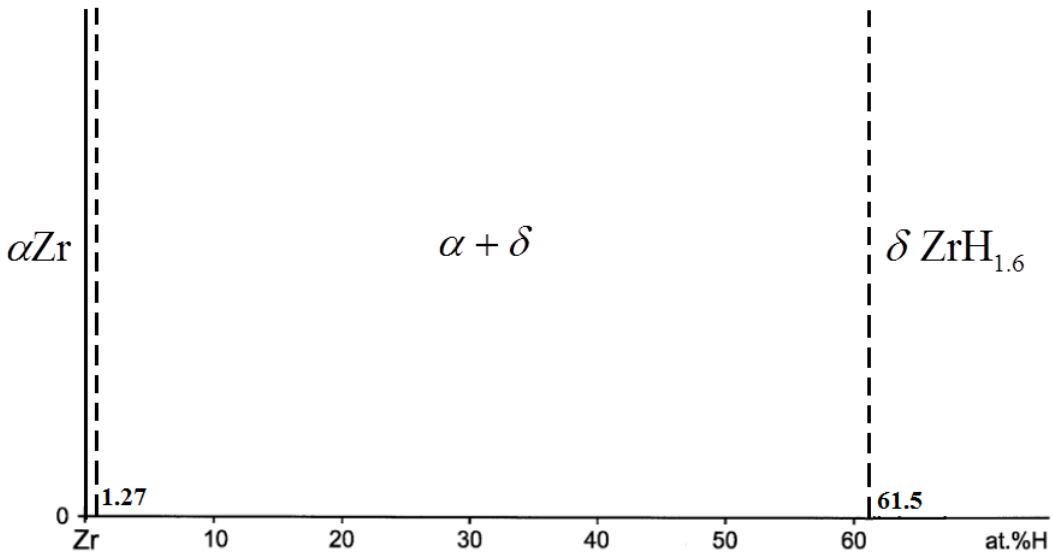

Figure 16 (a) The approximation to the Zr-H phase diagram used in this section. When hydrogen concentration reaches the maximum solubility in α-zirconium, the H atomic fraction is 1.27%. The chemical composition of δ-hydride is $ZrH_{1.6}$ whose H atomic fraction is 61.5%. No effects of temperature are included.

While the equilibrium conditions could be determined from the phase diagram. No rate information is provided. Here the assumption was made that diffusion of hydrogen is the rate-limiting step and the reaction rates are fast enough for equilibrium to be obtained in each time step. Rates of formation were included as a place-holder, but they will only affect the results if they are significantly slower than what we have assumed. This will have to wait for the correct lower-level results. The rates of hydride formation used in the analysis is shown in Fig. 17.

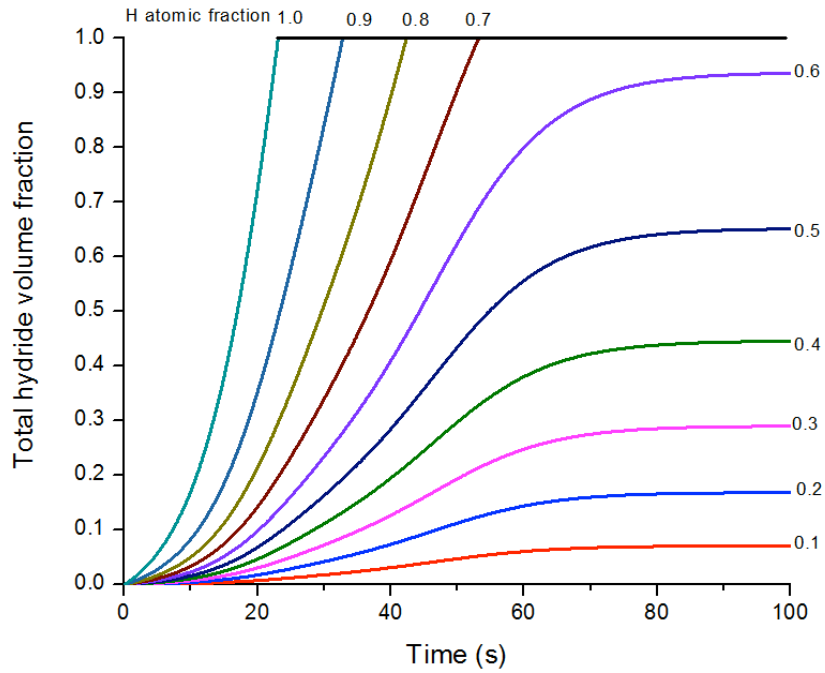

Figure 17 Volume fraction of hydride volume fraction plotted against time at different H atomic fractions. Based on the phase diagram of Fig. 17, there is no hydride formation when the H atomic fraction is below 1.27%. When theH atomic fraction is larger than 61.7%, the curve is truncated after the hydride volume fraction reaches 1. It has been assumed arbitrarily that it takes 100s for the α-zirconium-and-δ-hydride system reach equilibrium with a give H atomic fraction. The minimum time step in the gap analysis is 100s, so the system reaches equilibrium in every time increment.

6.1 Geometry

A 3-D model was constructed with four-fold symmetry. The dimensions of the model in the *x-y* plane are shown in Fig. 18. The outer and inner diameters of the cladding before service were taken to be 9.50 mm and 8.36 mm [Sham, 2012]. The diameter of the fuel was 8.20 mm, and the thickness of the grid was 0.46mm. The thicknesses of three parts along z-direction were 0.1mm. The motion of the top and bottom surfaces in *x-y* plane along the *z*-direction was constrained. Additionally, there was no frictional constraint at any interface. Contact elements were used at the interface between the pin and clad and at the interface between the clad and fuel to prevent interpenetration. An initial misfit of

0.09 mm was assumed between the outer surface of the cladding and the pin. The initial misfit in the mesh was allowed to reach equilibrium at 300 K for 10^6 s (approximately 10 days), using the creep model of Wang *et al.* [2012]. After this period of relaxation, the temperature and pressure boundary conditions appropriate for the first cycle of the reactor were applied for 100 seconds to allow the steady-state temperature to be reached with the creep mechanisms operating. Then, the calculation is allowed to start simulate the first cycle that lasts 5×10^7s.

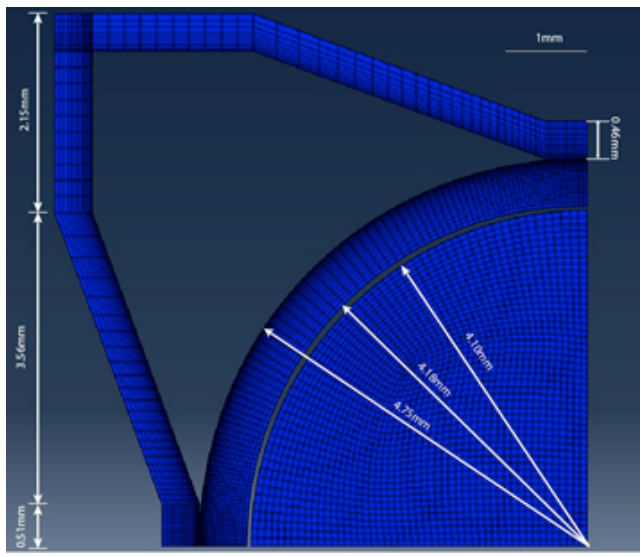

Figure 18 The 3-D mesh with quarter-plane symmetry used for the calculations of gap formation described in this report. The outer surfaces of the two straight segments at the top left-hand corner are rigidly constrained. The dimensions of the 3-D model in the *x*-*y* plane are shown in the figure. The thickness of the model along *z*-direction is 0.1mm.

6.2 Loading

In addition to the geometrical constraints discussed above, two types of loads were applied to the model as boundary conditions: a gauge pressure acting on the outside of the cladding arising from the difference in coolant pressure and the internal tube pressure; temperature gradients in the fuel arising from the fission, and across the cladding to the

coolant. The details of the two loads are described in the last report [Wang *et al.*, 2012]. Additionally, a hydrogen influx of 1×10^{-9} [ppm·m/s] was assumed on the outer surface of the cladding, the inner surface of the grid, and the unconstrained portions of the outer surface of the grid (as shown in Fig. 19).

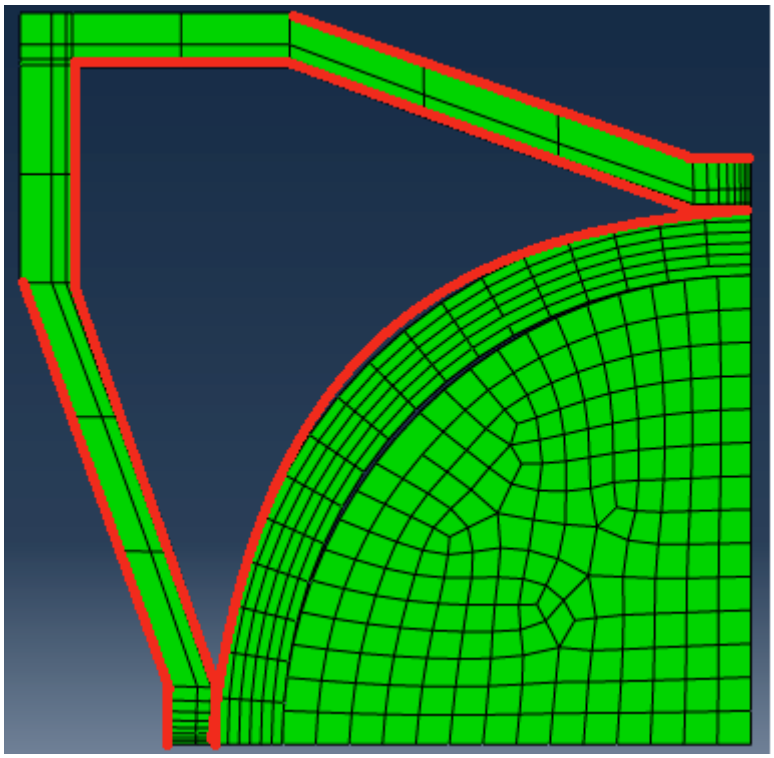

Figure 19 A hydrogen influx of 1×10^{-9} [ppm·m/s] is assumed on the red surface.

6.3 Material properties

All the mechanisms described in the last report [Wang *et al*., 2012] were included in this simulation except we also used the irradiation growth model described in this report. For this model, we assumed that the neutron flux was $6\text{x}10^{17}$ n/m^2, and the dislocation density in the zircaloy was $4.5\text{x}10^{14}$ m^{-2}. Again, it should be emphasized that there appear to be

no lower-level models that relate dislocation density to cold work and subsequent service and exposure to radiation flux and temperature. This would be needed for true multi-scale modeling of the irradiation growth process.

6.4 Simulation results

Calculations of the stress distribution and the evolution of the contact stress were done for the initial misfit of 0.09 mm, defined as the misfit between the outer diameters of the unstressed clad and the internal spacing between the unstressed grid at 300 K. Upon assembly at this temperature the stress distribution and contact is dominated by elasticity and dislocation glide (plasticity). This stress distribution was allowed to evolve for 10^6 s (after which any further changes in stress and deformation were negligible, within any reasonable timeframe that might be ascribed to the period before loading the fuel assembly in the reactor). The next step in the calculation involved the establishment of the steady-state temperature distribution. To enable an efficient numerical solution, this was done over a period of 100 s while permitting creep to occur. Then, the full simulation with all the processes of irradiation growth, fuel swelling, hydride formation, and creep were run for 5×10^7s corresponding to the first fuel cycle. (As this was just a demonstration, the calculation was run for a single cycle. rather than over all three cycles.) However, as a point of comparison, the calculations were run for two cases: one with hydride growth switched on, the other with it switched off.

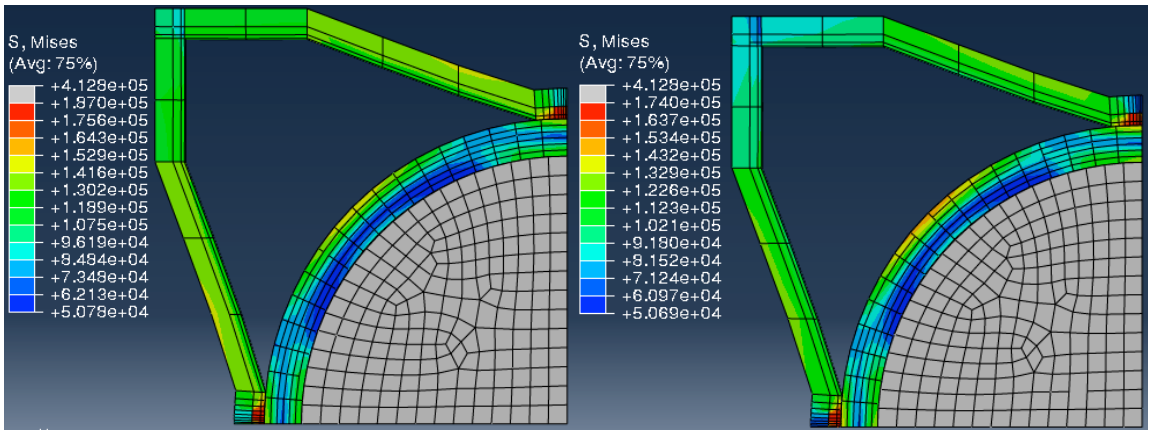

(a) **(b)**

Figure 20 von Mises stress distributions at the end of cycle one, 5×10^7s **(a)** with hydride formation **(b)** without hydride formation. In comparison to the case where hydride growth is switched off, the formation of hydride in the cladding and grid leads to a higher stress distribution.

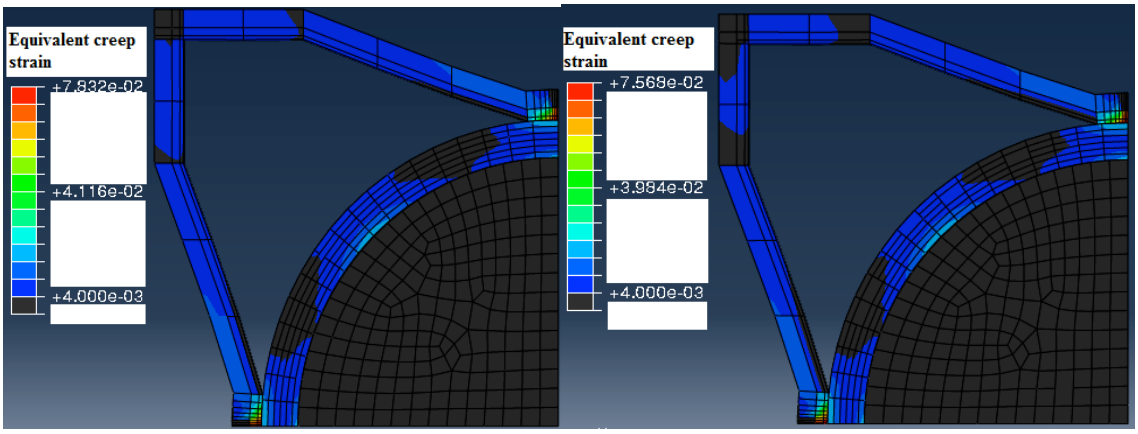

(a) **(b)**

Figure 21 Equivalent creep strains at the end of one thermal cycle; **(a)** with hydride formation **(b)** without hydride formation.. In comparison to the case where hydride growth is switched off, the formation of hydride in the cladding and grid leads to a higher equivalent creep strain, which is caused by the higher stress distribution,

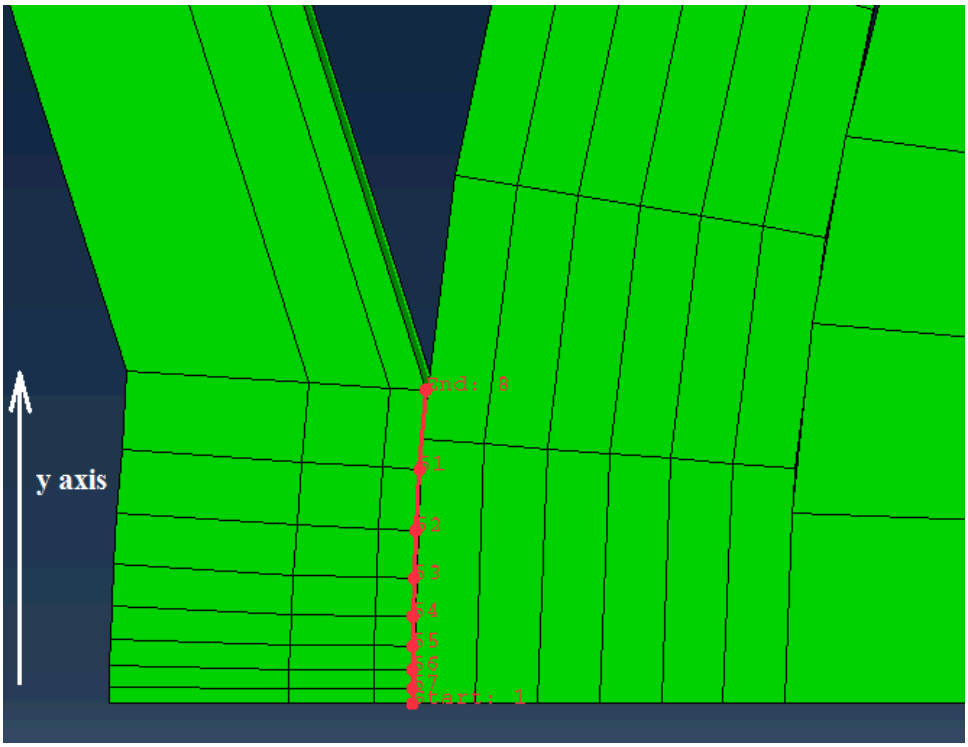

Figure 22 A detail of the contact area, indicating in red the nodes along which the contact stresses are analyzed. This is a deformed mesh, in which there is a stress across the contact, causing deformation of the cladding

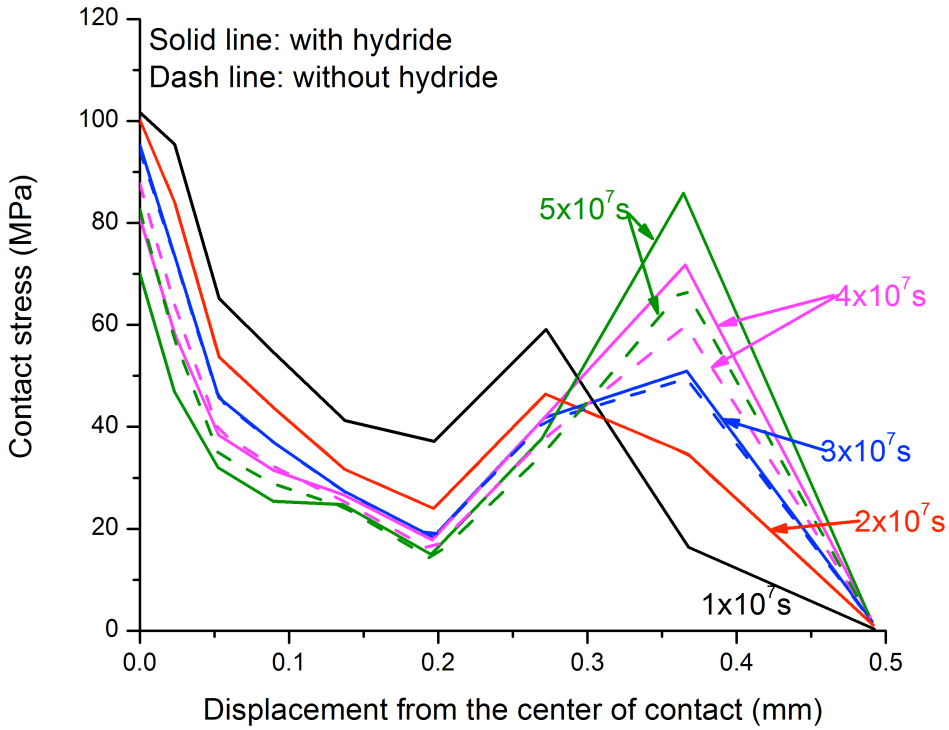

Figure 23 The evolution of the contact stress at the interface between the pin. With hydride forming in the cladding and grid, the contact stress at the interface is larger than that of the case where no hydride forms.

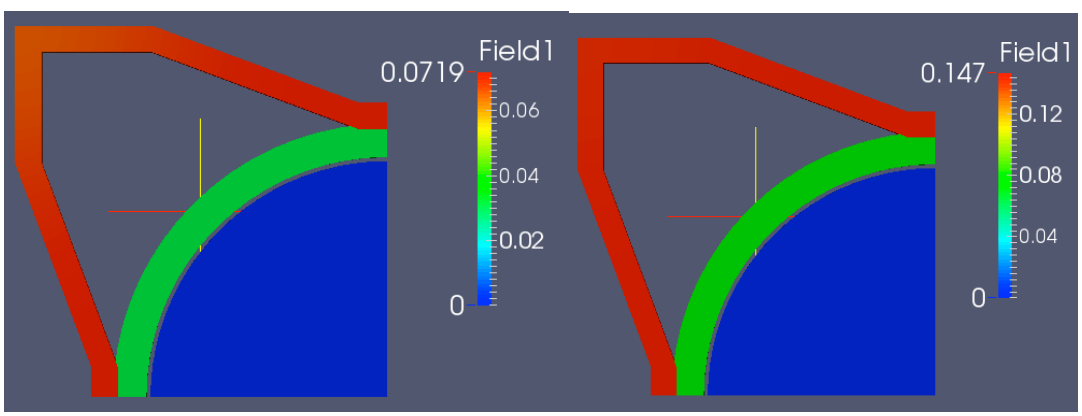

(a) **(b)**

Figure 24 The distribution of the volume fraction of hydride In this simulation, the hydride distribution is uniform in the grid and cladding after **(a)** 3×10^7 s **(b)** 5×10^7 s, owing to the relatively rapid diffusion of hydrogen in zirconium.

7. Future work

The following issues need to be addressed to have a working multi-scale model of hydride growth that can be incorporated into the GTRF problem.

1. A correct energy function for the interaction between H and Zr needs to be supplied to the phase-field level analysis, so that correct predictions for hydrogen solubility and equilibrium volume fractions of hydride are correctly predicted.

2. A set of results for single-crystal hydride formation at different levels of in-plane biaxial stress / temperature and hydrogen concentration that can be called upon by the FEM program is required.

3. Some results for the dissolution of hydride need to be developed, so that if conditions change resulting in excess hydride dissolution can occur.

4. An approach to model the situation where neighboring regions of the material are in local equilibrium between the hydrogen and hydride, but there is a gradient in total chemical potential between them. (The hydride will dissolve in regions of high volume fraction, and grow in the lower regions. This can be modelled by an apparent diffusion of hydride, but the rates are unknown.)

5. In the absence of complete lower-level data and models, the continuum model can be used by assuming that hydrogen diffusion, not the rate of hydride formation, is the rate-limiting process. The results of such an assumption have been incorporated in the GTRF model; however, it should be noted that the framework is capable of using the phase-field results to provide a smooth transition between diffusion-limited and rate-limited hydride formation.

6. With similar lower-level data, we expect it should also be possible to extend this framework to single crystal models of oxide formation, or irradiation growth.

The following basic issue needs to be addressed at the lower length scale if models of irradiation growth are to be incorporated into finite-element models: how does the dislocation density vary with service?

Acknowledgements

We are very grateful for the collaborations with Ms. Jokisaari and Prof. Thornton at UM on the hydride evolution problem, and look forward to continuing this in the coming year.

References

C.M. Allison, G.A. Berna, R. Chambers, E.W. Coryell, K.L. Davis, D.L. Hagrman, D.T. Hagrman, N.L. Hampton, J.K. Hohorst, R.E. Mason, M.L. McComas, K.A. McNeil, R.L. Miller, C.S. Olsen, G.A. Reymann, and L.J. Siefken. "SCDAP/RELAP5/MOD3.1 Code Manual Volume IV: MATPRO -- A Library of Materials Properties for Light-Water-Reactor Accident Analysis (Matpro)". D.T. Hagrman, NUREG/CR-6150, EGG-2720, Volume IV. 1993.

G. J. C. Carpenter, R. A. Murgatroyd, A. Rogerson, and J. F. Watters, "Irradiation growth of zirconium single crystals", *Journal of Nuclear Materials*, **101**, p. 28-37, 1981.

G. J. C. Carpernter, R. H. Zee, and A. Rogerson, "Irradiation growth of zirconium single crystals: a review", *Journal of Nuclear Materials*, **159**, p. 86-100, 1988.

A. R. Causey, R. A. Holt, N. Christodoulou, and E. T. C. Ho. "*Irradiation-enhanced deformation of Zr-2.5Nb tubes at high neutron fluences". Zirconium in the Nuclear Industry: Twelfth International Symposium, ASTM STP 1354*, G.P. Sabol and G.D. Moan, Eds., p. 74-85, 2000.

X. H. Guo, S. Q. Shi, Q. M. Zhang, X. Q. Ma, "An elastoplastic phase-field model for the evolution of hydride precipitation in zirconium. Part I: Smooth specimen," *Journal of Nuclear Materials*, **378**, p. 110-119, 2008.

J. E. Harbottle and R. M. Cornell, "Irradiation Growth in Zircaloy", *Nuclear Engineering and Design*, **42**, p. 423-429, 1977.

R. A. Holt, "Effect of Microstructure on Irradiation creep and Growth of Zircaloy Pressure Tubes in Power Reactors", *Journal of Nuclear Materials*, **82**, p. 419-429, 1979.

R. A. Holt, "Microstructure dependence of irradiation creep and growth of zirconium alloys", *Journal of Nuclear Materials*, **90**, p. 193-204, 1980.

R. A. Holt and R. W. Gilbert, "<c> Component Dislocations in Annealed Zircaloy Irradiated at About 570K", *Journal of Nuclear Materials*, **137**, p. 185-189, 1986.

R. A. Holt and R. G. Fleck. "*The effect of temperature on the irradiation growth of cold-worked Zr-2.5Nb". Zirconium in the Nuclear Industry: Eighth International Symposium, ASTM STP 1023*, L.F.P.V. Swam and C.M. Eucken, Eds., p. 705-721, 1989.

E. F. Ibrahim and J. E. Winegar, "Dimensional changes of unstressed Zircaloy-2 and Zr-2.5% Nb specimens in a fast neutron flux", *Journal of Nuclear Materials*, **45**, p. 335-338, 1972/73.

M. Leger and R. G. Fleck. "*Irradiation growth in Zr-2.5Nb". Zirconium in the Nuclear Industry: Sixth International Symposium, ASTM STP 824*, D.G. Franklin and R.B. Adamson, Eds., p. 409-426, 1984.

R. A. Murgatroyd and A. Rogerson, "An assessment of the influence of microstructure and test conditions on the irradiation growth phenomenon in zirconium alloys", *Journal of Nuclear Materials*, **90**, p. 240-248, 1980.

J. D. Parker, V. Perovic, M. Leger, and R. G. Fleck. "*Microstructureal effects on the irradiation growth of Zr-2.5Nb". Zirconium in the Nuclear Industry: Seventhth International Symposium, ASTM STP 939*, R.B. Adamson and L.F.P.V. Swam, Eds., p. 86-100, 1987.

A. Rogerson, "Irradiation growth in zirconium and its alloys", *Journal of Nuclear Materials*, **159**, p. 43-61, 1988.

S. Sham, Oak Ridge National Laboratory, "Geometry for gap evolution", *MPO Presentation*, Feb 9, 2012.

R. N. Singh, P. Stahle, A. R. Massih and A. A. Shmakov,"Temperature dependence of misfit strains of delta-hydrides of zirconium." *Journal of Alloys and Compounds,* **436**, p.150-154, 2007.

M. S. Veshchunov and A. V. Berdyshev, "Modelling of hydrogen absorption by zirconium alloys during high temperature oxidation in steam", *Journal of Nuclear Materials*, **255** p. 250-262, 1998.

H. Wang, Z. Hu, W. Lu and M. D. Thouless, "Evolution of the Gap and Contact Pressure between a Fuel Rod and Grid during Operation in a PWR", Report to CASL / MPO - August 2012.

H. Wang, Z. Hu, W. Lu and M. D. Thouless, "A mechanism-based framework for the numerical analysis of creep in zircaloy-4." *Journal of Nuclear Materials,* **433**, 188-198, 2013.